Supplementary Material : Isostructural phase transition of Fe_2O_3 under laser shock compression

A. Amouretti*
IMPMC, Sorbonne Université, UMR CNRS 7590, MNHN, 75005 Paris, France and
Graduate School of Engineering, Osaka University, Suita, Osaka 565-0871, Japan

C. Crépisson,† S. Azadi, T. Campbell, A. Forte,
T. Gawne, P. Heighway, Y. Shi, and J. S. Wark
Department of Physics, Clarendon Laboratory,
University of Oxford, Parks Road, Oxford OX1 3PU, UK

F. Brisset
Université Paris-Saclay, CNRS, Institut de chimie
moléculaire et des matériaux d'Orsay, Orsay 91405, France

D. Cabaret, G. Fiquet, F. Guyot, and J. Pintor
IMPMC, Sorbonne Université, UMR CNRS 7590, MNHN, 75005 Paris, France

D. A. Chin, G. W. Collins, L. Hansen, D. N. Polsin, and E. Smith
University of Rochester Laboratory for Laser Energetics, Rochester, NY, USA

E. Heriprë
PIMM, Arts et Metiers Institute of Technology,
CNRS, CNAM, HESAM University,
151 boulevard de l'Hopital, 75013 Paris, France

E. Cunningham, H. J. Lee, and B. Nagler
SLAC National Accelerator Laboratory,
2575 Sand Hill Rd, Menlo Park, CA 94025, USA

D. McGonegle
AWE, Aldermaston, Reading, RG7 4PR, United Kingdom

G. Rousse
CSE Lab, UMR 8260, Collège de France, 75231 Paris Cedex 05, France and
Sorbonne Université, 4 place Jussieu, 75005 Paris, France

S. M. Vinko
Department of Physics, Clarendon Laboratory,
University of Oxford, Parks Road, Oxford OX1 3PU, UK and
Central Laser Facility, STFC Rutherford Appleton Laboratory, Didcot OX11 0QX, UK

M. Harmand
IMPMC, Sorbonne Université, UMR CNRS 7590, MNHN, 75005 Paris, France and
PIMM, Arts et Metiers Institute of Technology,
CNRS, Cnam, HESAM University,
151 boulevard de l'Hopital, 75013 Paris, France

(Dated: March 22, 2025)

---

[*] AmourettiA@eie.eng.osaka-u.ac.jp

[†] celine.crepisson@physics.ox.ac.uk

A. Experimental setup

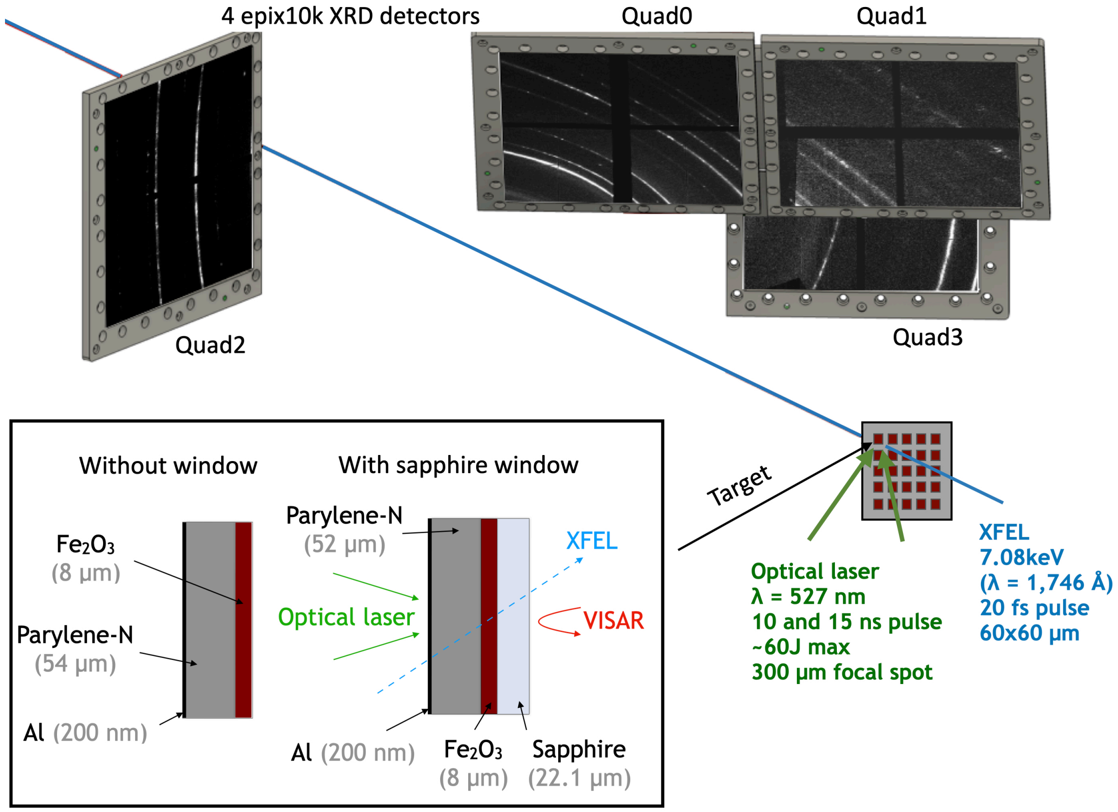

FIG. S1. Experimental set-up for in-situ x-ray diffraction under laser-driven shock compression performed at MEC (Matter in Extreme Condition) beamline, LCLS. The angular range is 20 to 100 degrees scattering angle and the azimuthal range is approximately 90 to 220 degrees for the 3 detectors on the right and 0 to 60 degrees for the detector on the left. Targets without a sapphire window are probed slightly before breakout time to avoid release and as such ambient peaks remain visible (Fig. 1 of the main paper). Targets with a sapphire window are probed when the sample is entirely shocked. A very small amount of ambient peak is however visible for those targets (Fig. 1 of the main paper), which can be explained by the halo surrounding the x-ray beam described in [1].

Two different target designs were used. The first design contained an 8 μm layer of Fe_2O_3 sandwiched between a 22.1 μm sapphire window on one side, and a 54 μm layer of parylene-N on the other. The sapphire window allows for a direct measurement of the particle velocity, and thus enables directly extracting the Hugoniot pressure over a large range of laser intensities. The second design consists of 8 μm of Fe_2O_3 deposited on 54 μm of parylene-N and aims to optimize the XRD signal (no contribution from sapphire Bragg spots). A 200 nm aluminum flash coating was applied to the front face of all targets to minimize direct heating by the laser prepulse. The Fe_2O_3 was deposited via Physical Vapor Deposition (PVD). Deposition on a glass substrate was used to characterize our samples and we observed a polycrystalline structure of columnar crystallites with a preferential orientation along the (300) lattice planes, perpendicular to the shock wave propagation in our setup geometry (see Figs. S1-S11). Ambient XRD measurements were taken prior to every shock, a slight variation in relative peak intensity is observed linked with variability in initial texture (see Fig. S2 right).

B. Fe_2O_3 sample

Samples are composed of 0.5 to 1.5 um large Fe2O3 columns perpendicular to the Parylene-N or sapphire substrate as shown in Figure B. No difference is observed between deposition on Parylene-N, sapphire or Si substrates. No voids are observed between the columns, suggesting the absence of porosity in the material. The fractures observed in the image are due to the preparation of the section, which involves cutting the Si substrate in two pieces.

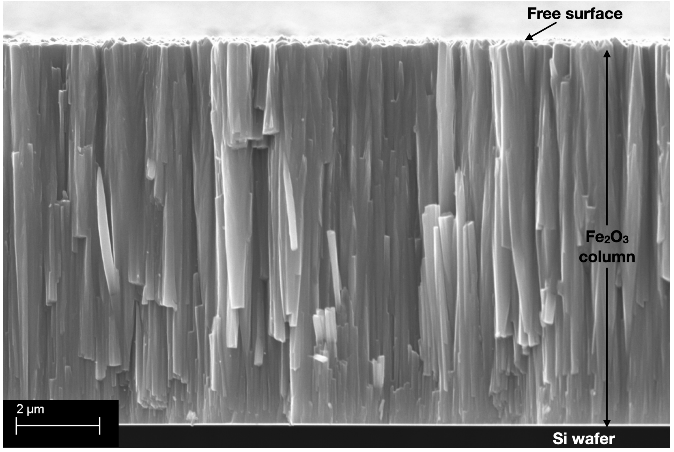

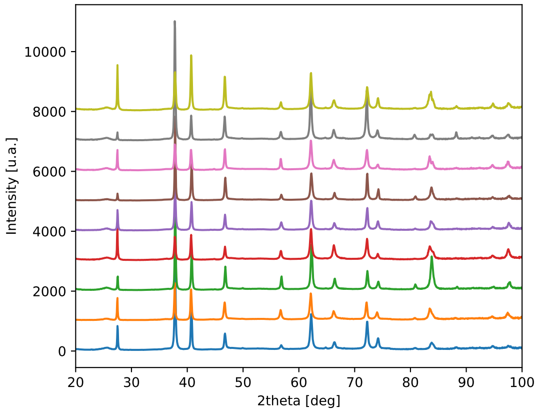

C. Preferential orientation of Fe_2O_3 deposition

To characterize the preferential orientation of the Fe_2O_3 deposition, we performed x-ray diffraction measurements using Bragg-Brentano geometry. In Figure S3, the (300) Bragg reflection has a significantly higher intensity than the standard hematite powder without texture and preferential orientation. Peak intensities for standard hematite powder are given at the bottom of the figure in blue. This indicates that the (300) lattice planes, shown in Figure S3 on the right are mostly parallel to the deposition and thus perpendicular to the shock front.

In order to better define the preferential orientation of our deposition, we performed two Rietveld refinements, shown in red in figure S3: at the top without texture or preferential orientation taken into account and at the bottom using a March-Dollase function to account for preferential orientation, modeling axially symmetric flat-plate samples, composed of rod crystallites [4], i.e. with a columnar texture. Without texture or preferential orientation, the refinement has a $Rwp = 13.9$ %, and the (300) peak intensity is not fitted correctly. With the March-Dollase function, the coefficient obtained is $Rwp = 4.5\%$ with a March-dollase ratio of $r = 0.183$, and the (300) peak intensity is seen to be well reproduced indicating a preferential orientation along the (300) planes. We can however see that some peak's intensities are not perfectly accounted for with March-Dollase function implying that a more complex treatment of the texture and preferential orientation is needed.

D. Electron Backscattered Diffraction (EBSD) measurements

We performed EBSD measurements on two Fe_2O_3 samples prepared for the experiment: one deposited on a sapphire window (fig. S4 and fig. S5(a) top) and one deposited on Parylene-N (fig. S5(a) bottom). EBSD data were acquired on a Zeiss Supra 55 VP in low vacuum mode and fitted with an EDAX Velocity EBSD system. The high voltage was 20 kV, the beam current was about 4 nA and the nitrogen pressure in the chamber was set at 25 Pa, to avoid charging effects. Acquisitions were done either in the plane perpendicular to the growing direction for Fe_2O_3 deposited on sapphire (fig. S4) at a step size of 20 nm or on the plan of the sample for both samples (Fig. S5(a) top - step 30 nm, and Fig. S5(a) bottom - step 40 nm). The [0001] direction (Fig. S4) is parallel to the section observed, which means

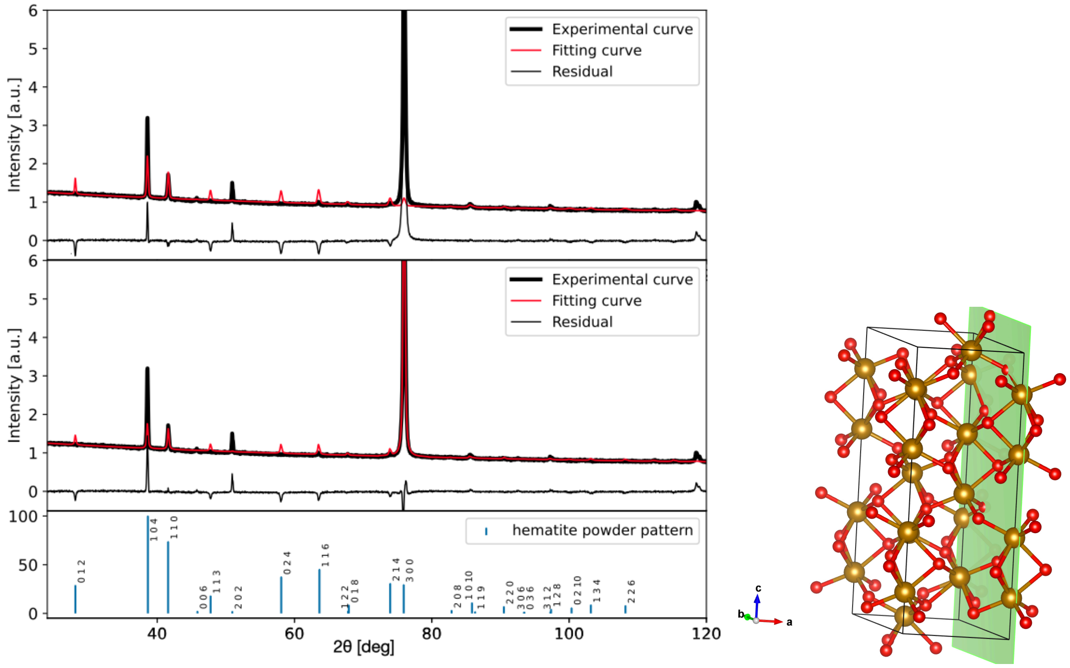

FIG. S3. **Left :** Rietveld refinements of X-ray diffraction profile of Fe_2O_3 deposition on glass substrate acquired in Bragg-Brentano reflection geometry using a Cobalt X-ray source ($\lambda = 1.789$ Å). Refinement was performed using MAUD software [2]. The experimental pattern is shown by a thick black line, the refinement by a thick red line, and the residual is shown as a thin black line underneath. On the fit of the upper figure, no preferred orientation has been taken into account. On the pattern below, preferred orientation was taken into account using a March-Dollase function as implemented in MAUD indicating a preferential orientation primarily along the (300) lattice plane. The coefficient obtained is Rwp = 4.5% and the March-Dollase ratio is equal to $r = 0.183$. Fitted lattice parameters are: a = 5.038 Å and c = 13.827 Å. Fitting of peak-broadening gives an average crystallite size of 638 nm. The peaks at the bottom represent the calculated pattern (position and intensity of peaks) for standard hematite powder [3]. **Right :** Fe_2O_3 crystal structure showing the (300) lattice plane in green for which a preferential orientation is observed.

that the (0001) (i.e. the (001)) plane is parallel to the substrate. This result is consistent with Rietveld refinements presented in section C. For both Fe_2O_3 deposited either on sapphire or Parylene-N the $[01\bar{1}0]$ and the $[1\bar{1}00]$ directions are observed to be parallel to the surface of the sample. The preferential orientation observed for the surface was not accounted for in the Rietveld refinement and could explain the remaining discrepancies between the fit and the measurement. We can see that both samples have the same preferential orientation,

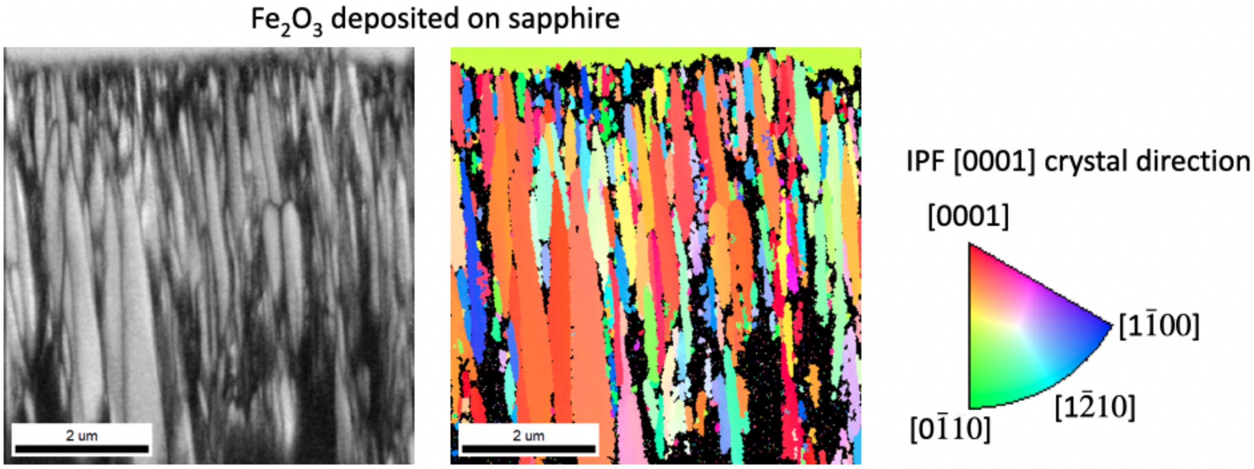

FIG. S4. Pattern quality image showing the elongated grains along the growing direction (left) and orientation map (inverse pole figure) (right) showing a preferential orientation overall along the [0001] direction.

with pole figures characteristic of fiber texture (fig. S5(b)). Eventually, slight variations are observed in preferential orientation within the samples, which can explain the variation observed on ambient samples (fig. B - right).

E. Hydrodynamic simulation

For targets with sapphire window, hydrodynamic simulations displayed in figure S6 show that the shock wave is entering Fe_2O_3 layer at around 6 ns after crossing the parylene-N layer. Due to the strong difference in impedance between the parylene-N and Fe_2O_3 the pressure is significantly higher in the Fe_2O_3 layer compared to the parylene-N layer. The shock wave then leaves the Fe_2O_3 layer at 7 ns to enter the sapphire window. As the impedance of Fe_2O_3 and sapphire are similar (see green and black curves of figure S8 - right), the wave reflected back into Fe_2O_3 at the sapphire - Fe_2O_3 interface induces a pressure close to that of the incident wave arriving from Fe_2O_3 (by ±5 GPa). The compression is thus shown to be maintained till around 8.5 ns before the arrival of the expansion wave from the parylene-N layer. Homogeneous shock conditions along the Hugoniot can thus be probed between 7 and 8.5 ns.

Similarly, for targets without sapphire windows, hydrodynamic simulations displayed in Figure S6 show that the shock wave enters the Fe_2O_3 layer at around 6 ns and leaves the

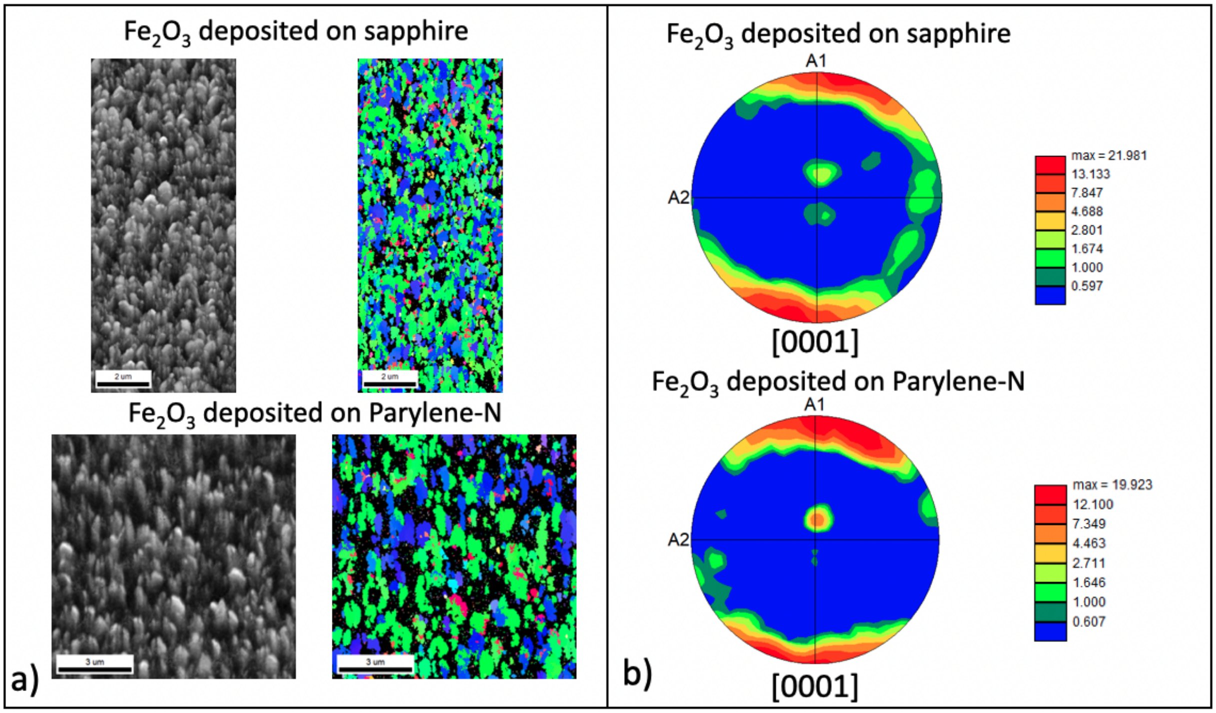

FIG. S5. (a) Patterns quality image (left) and orientation map (right) on the sample plane. (b) Related pole figures to the orientation map are displayed in fig S4. Although the investigated area is small a strong fiber texture is observed.

layer at 7 ns. An expansion wave is then directly reflected from the air back into the Fe_2O_3 layer, arriving at around 8 ns leading to a series of compression/expansion into the Fe_2O_3 layer. To probe homogeneous shock conditions along the Hugoniot the X-ray probe must be synchronized just before the shock wave exits the Fe_2O_3 layer at 7 ns.

F. Pressure determination

For targets with a sapphire window, particle velocity $u_p(Sa)$ was determined from the Fe_2O_3/Sapphire interface by VISAR. However, a corrected refractive index for shocked Sapphire needs to be taken into account. To do so, we use results from Cao et *al.* [6]. In this paper, a relation between the true particle velocity (called here the sapphire particle velocity $u_p(Sa)$) and the apparent particle velocity (corresponding to the Fe_2O_3/Sapphire interface velocity measured by VISAR in our experiment) is obtained for a wavelength of 1550 nm (see figure S7) and up to 210 GPa. As the LCLS VISAR used green light of 527 nm [7], we multiply the apparent particle velocity from Cao et *al.* [6] by a fac-

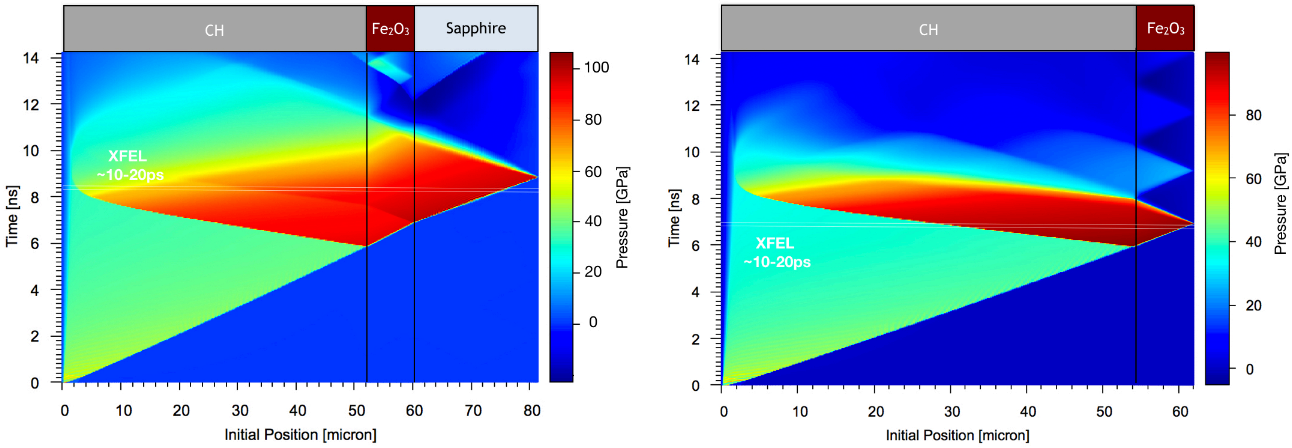

FIG. S6. Hydrodynamic simulations performed with MULTI [5] for target with sapphire window (left) and without window (right) as shown in Figure experimental setup. Numerical laser intensity is 1.2e12 W/cm^2 (corresponding experimental intensity of around 2.5e12 W/cm^2) with flat top laser pulse profile of 10 ns duration and 527 nm wavelength. At this intensity, the typical pressure in shocked Fe_2O_3 is 90 GPa. SESAME 7592 (with an initial density of 1.044 g/cm^3), SESAME 7440 (5.008 g/cm^3), and SESAME 7411 (3.97 g/cm^3) are used in the hydrodynamic simulation to model equation of state of parylene-N, Fe_2O_3, and sapphire, respectively.

tor of $n_0^{527nm}/n_0^{1550nm} = 1.770/1.745 = 1.014$, before fitting by a third order polynomial ($K_0 + K_1 x + K_2 x^2$) the true particle velocity versus the re-scale apparent particle velocity (as shown in figure S7). This relation has then been applied to all our Fe_2O_3/Sapphire interface velocity values to get $u_p(Sa)$ for each shot. The error on the $u_p(Sa)$ is set as $\delta u_p(Sa) = 0.05 * 1.9890/n_0^{527nm} = 0.06$ km/s, where 1.9890 km/s is the smaller VISAR sensitivity used in our experiment. If the two velocities extracted from VISAR1 and 2 were too different, we used the absolute difference between these two velocity values as uncertainty.

The pressure was then determined in Fe_2O_3 from $u_p(Sa)$ by using the impedance matching method, with SESAME 7440 and 7411 for Fe_2O_3 and sapphire Hugoniot respectively. The method is illustrated in figure S8. As sapphire impedance is slightly higher than Fe_2O_3 impedance, a reshock is created in Fe_2O_3, and the pressure is then slightly higher. We make use of the symmetrical Hugoniot and the single Hugoniot approximation for the Fe_2O_3 polar. This approximation is valid here, as the two Hugoniot curves of Fe_2O_3 and sapphire are extremely close.

For targets without sapphire windows, the free surface velocity was determined by VISAR.

The shock particle velocity u_p was then extracted using the following relation resulting from "weak shock" approximation $u_p = u_{fs}/2$ [8] (for pressure up to 116 GPa). The uncertainty for u_p, in the same way as for the targets with windows, is set as $\delta u_p = 0.05 * 1.9890/2 =$ 0.05 km/s. The pressure and its uncertainty were then determined from u_p and δu_p by using Fe_2O_3 Hugoniot relations [9].

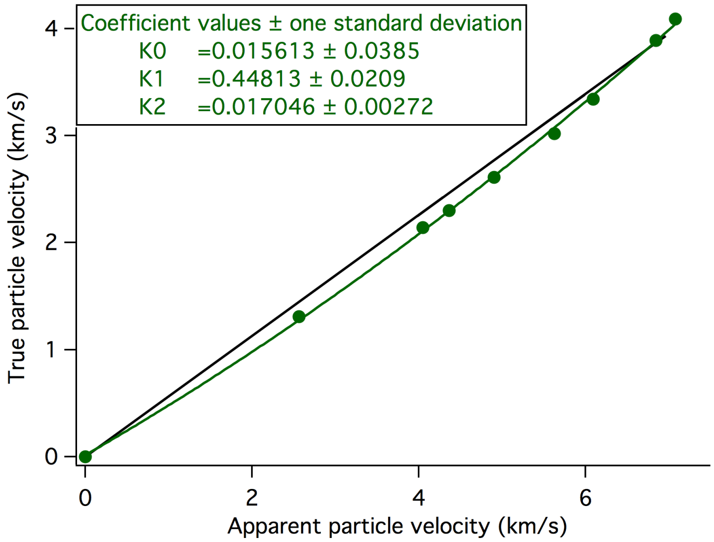

FIG. S7. Relationship between true particle velocity in sapphire and apparent particle velocity. Green dots correspond to data from Cao et *al.* [6] corrected for LCLS VISAR wavelength (527 nm) (see text) and the green line corresponds to a 3rd-degree polynomial fit ($K_0 + K_1 x + K_2 x^2$) of those data. The black line corresponds to the relation without sapphire index correction, that is constant refractive index equal to $n_0^{527nm} = 1.77$.

G. Evaluation of lattice parameters

The lattice parameters a and c, as well as the unit cell volume V, were determined by adjusting lattice parameters of a corundum structure [3] and matching theoretical peaks positions to experimental peaks position, more specifically the (110) and (104) reflections. By comparing the cell parameters a and c and volume V obtained via this method with those obtained by Le Bail fitting for shots 707 and 715 (Figure 2), we set the uncertainty to 0.03 Å for a, 0.02 Å for c and 4 Å^3, for the volume.

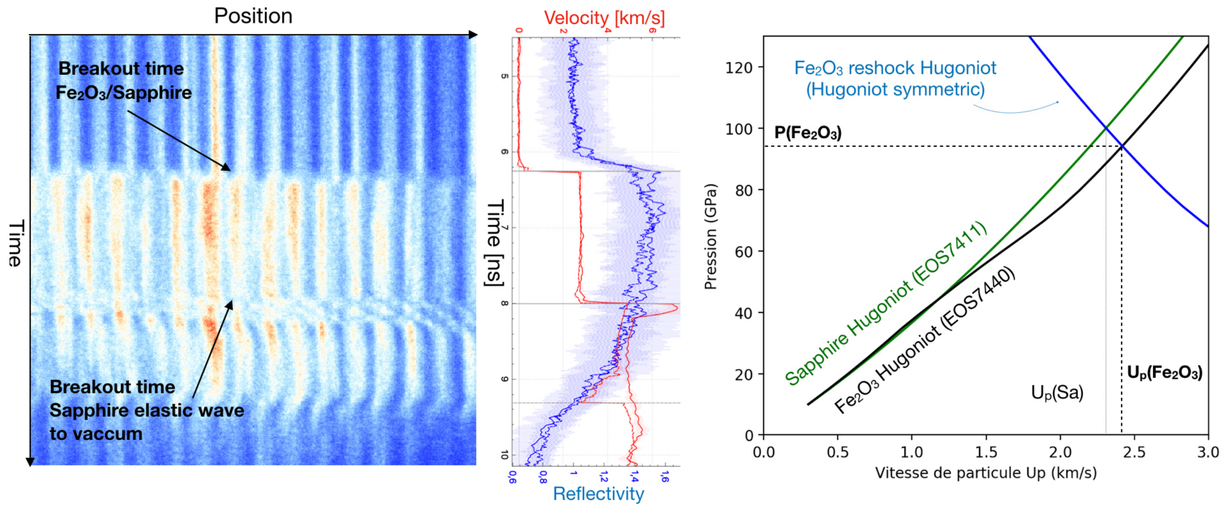

FIG. S8. **Left -** Example of a VISAR image for a target with a sapphire window. **Middle -** Velocity at the Fe_2O_3/Sapphire interface is determined based on the fringe displacement of the VISAR image, by using the free software Neutrino for analysis [10]. **Right -** Calculation of pressure and particle velocity in Fe_2O_3 using the impedance mismatch method.

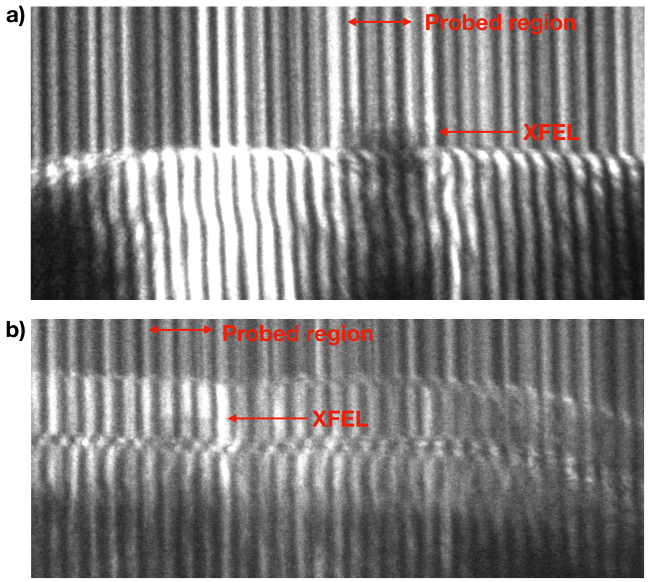

FIG. S9. VISAR images of shots realized on targets without windows a) and targets with sapphire windows b), respectively shots 705 and 588. Due to the high brilliance of the XFEL during those shots, we can observe the XFEL trace by a slight change of reflectivity (because of the Fe_2O_3 rear surface damage), and therefore define the probed position for each kind of target.

H. Wave splitting on VISAR data

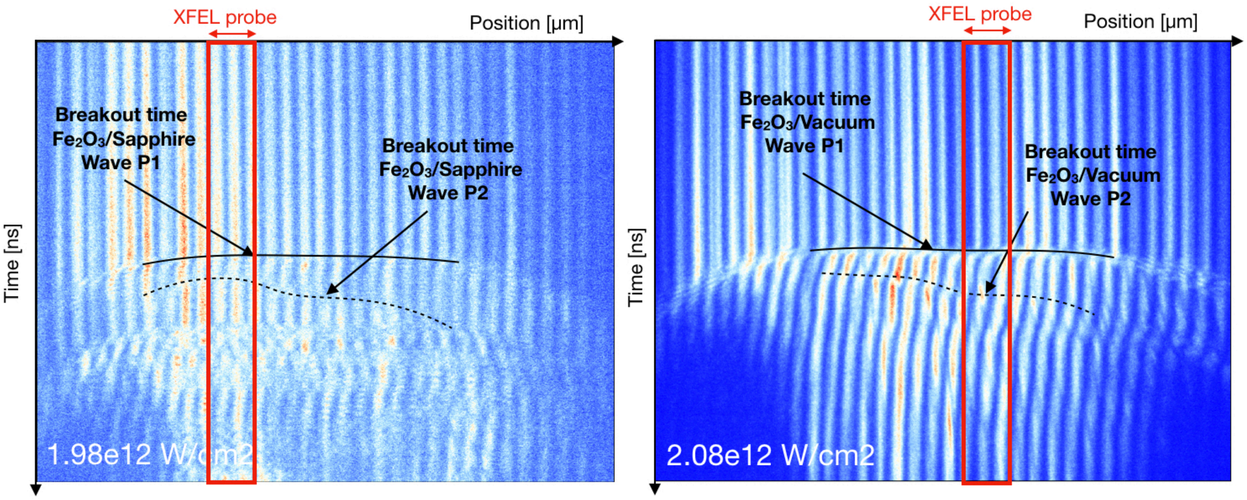

FIG. S10. Observation of a double-waves structure on VISAR image. VISAR image from a target with a sapphire window subjected to a laser intensity of 1.98e12 W/cm^2 (left figure) and VISAR image from a target without a sapphire window corresponding to a laser intensity of 2.08e12 W/cm^2 (right figure). The time at which the P1 wave and the P2 wave leave the Fe_2O_3 layer is indicated by a plain and a dotted line, respectively. P1 wave is associated to α-Fe_2O_3 phase and P2 to α'-Fe_2O_3. Non-planar shape of the P2 front is roughly reproduced for all the data and could be explained by different phenomena. (1) It could be due to the systematic laser profile inhomogeneity: the shock velocity of the P2 wave is more sensitive to non-planarity than the P1 wave, leading to inhomogeneity mostly observable in the P2 wave profile. (2) It could indicate a direction of shock wave propagation influenced by the anisotropy of our sample [11]. The XFEL probe region however is small enough compared to non-planarity to consider the P2 shock front planar at the probe position.

When two waves are present in the VISAR profile, P1 and P2 corresponding respectively to α-Fe_2O_3 and α'-Fe_2O_3 we determine the pressure as detailed below. We note u_{p1} the particle velocity of the first wave corresponding to the transition pressure P_1, and u_{p2} the velocity of the second wave corresponding to the phase transformation wave compressing the sample to the pressure P_2. The pressure associated with the P2 wave is determined using a two-jumps Rankine-Hugoniot relation [12]:

$$P_2 = P_1 + \rho_0(U_{S2} - u_{p1})(u_{p2} - u_{p1}) \quad \text{with} \quad U_{S2} = \frac{u_{p2} - u_{p1}\frac{\rho_1}{\rho_2}}{1 - \frac{\rho_1}{\rho_2}} \tag{ES1}$$

With ρ_1 and ρ_2 evaluated using the x-ray diffraction data. ρ_1 is the density of the α phase and ρ_2 is the density of the high pressure phase α'.

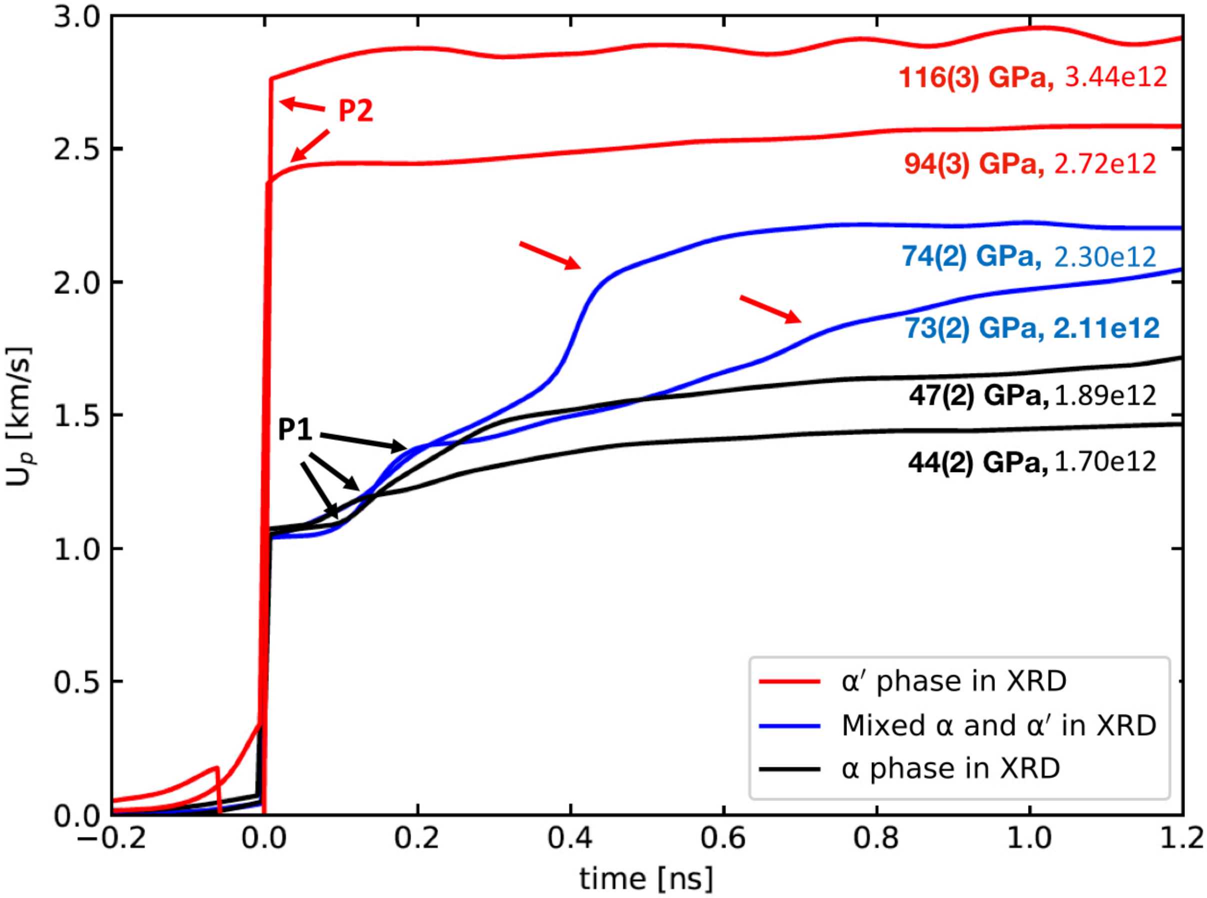

FIG. S11. Particle velocities for the targets without sapphire window. Particle velocity is determined from the free surface velocity measured at the Fe_2O_3 rear side by VISAR. Similarly to targets with sapphire window (discussed in the main paper and displayed in Figure 3), when both α-Fe_2O_3 and α'-Fe_2O_3 are observed in x-ray diffraction (blue curves), a double wave structure is clearly observed and is understood as the signature of the phase transition with P1 associated to α-Fe_2O_3 phase and P2 to α'-Fe_2O_3. The velocity profiles below and above the phase transition are also shown, respectively with black and red color. 0 ns is defined when the shock leaves the Fe_2O_3 layer. The pressure indicated corresponds to P1 for the two lowest intensity shots (1.7e12 and 1.89 W/cm^2) and to P2 for all other velocity profiles (2.11e12, 2.30e12, 2.72e12, and 3.44e12 W/cm^2).

I. Fe_2O_3 diffuse signal at 122(3) GPa

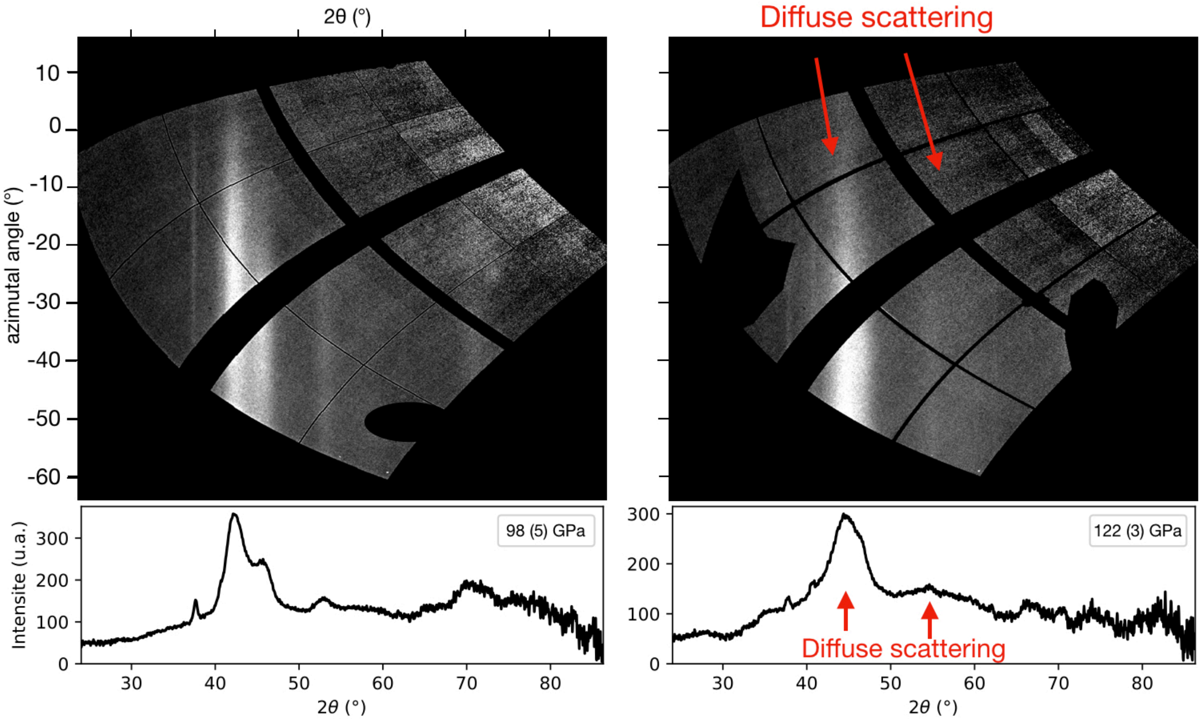

FIG. S12. 2D diffraction image from the main detector (Quad0) showing the appearance of diffuse features at 122(3) GPa on a target with Sapphire window. Sapphire spots have been masked. For comparison, a sample showing no diffuse feature at 98(5) GPa is also shown for a target with a sapphire window. Corresponding integrated diffraction profiles are shown below. XRD study of higher pressure Fe_2O_3 under shock showing diffuse scattering has been performed elsewhere [13].

J. High-pressure phase identification

We tested high-pressure phases previously reported by studies of Fe_2O_3 under static compression against our high-pressure diffraction patterns. In this aim we compare an integrated x-ray diffraction profiles from this study for a run at 94(2) GPa on a target without sapphire with calculated x-ray diffraction profiles for the following phases: α-Fe_2O_3[14], η-Fe_2O_3[14], θ-Fe_2O_3[14], ι-Fe_2O_3 [14], ζ-Fe_2O_3, h-Fe_3O_4 [15], FeO_2 [16], Fe_5O_6 [17], Fe_4O_5 [18], Fe_5O_7 [14], $Fe_{25}O_{32}$ [14]. We use a constant broadening of 1.25° to match our experimental data. Some residual peaks from ambient α-Fe_2O_3 are visible and indicated by green dotted

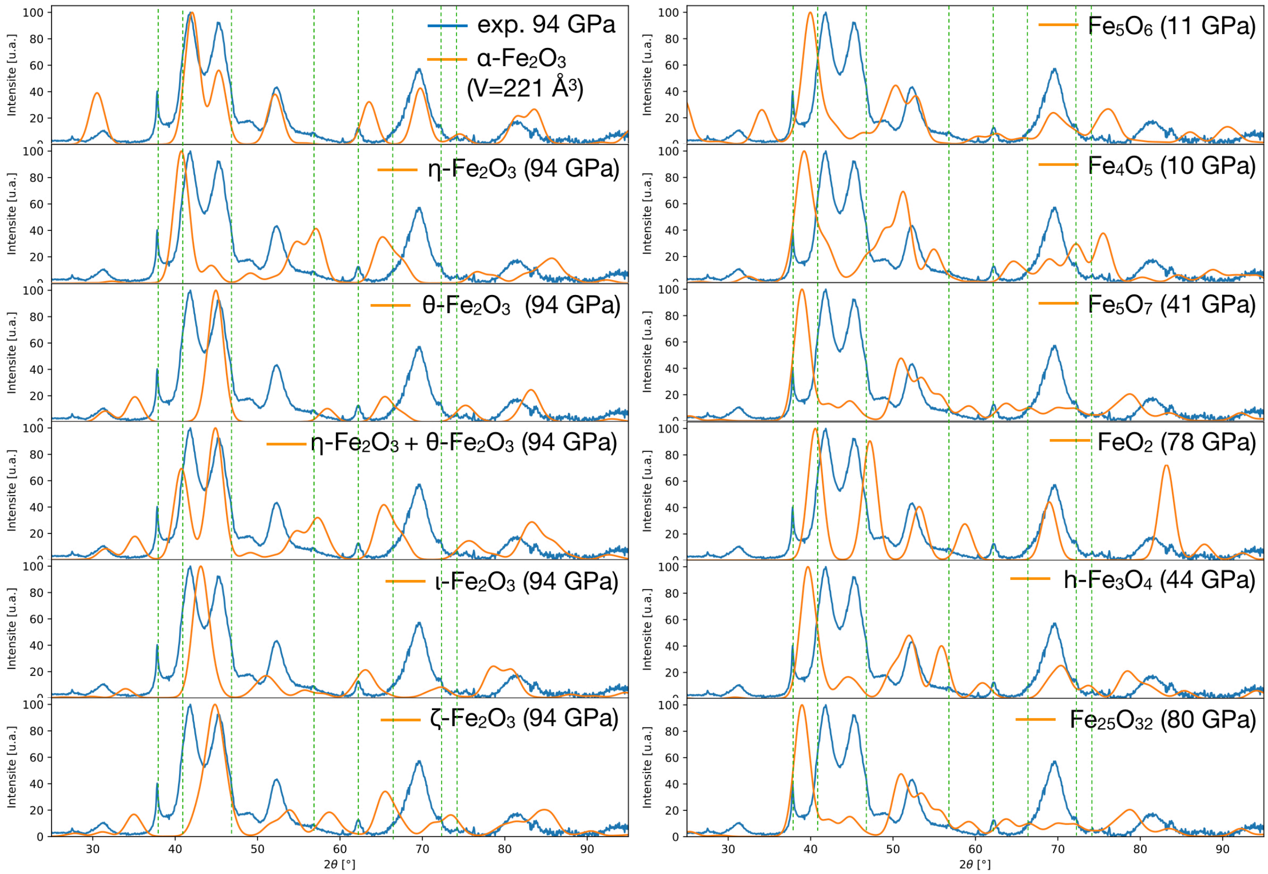

FIG. S13. Test to identify the peaks of the high-pressure phase (α'-Fe_2O_3 phase) by different high-pressure phases found in the literature. The shot corresponds to a shot on target without a sapphire window on which Le Bail refinement was carried out, 94 GPa, according to VISAR, drawn in blue. Green dotted vertical lines refer to remaining ambient alpha-Fe2O3 peaks. These phases correspond to : α-Fe_2O_3[14], η-Fe_2O_3[14], θ-Fe_2O_3[14], ι-Fe_2O_3 [14], ζ-Fe_2O_3, h-Fe_3O_4 [15], FeO_2 [16], Fe_5O_6 [17], Fe_4O_5 [18], Fe_5O_7 [14], $Fe_{25}O_{32}$ [14]. The alpha phase of hematite matches the peaks best, in terms of intensity and position. None of the other phases explains all of the peaks, both position and relative intensity.

vertical lines in figure S13. Cell parameters of the simulated phases were adjusted for a pressure of 94 GPa using available equations of state (left column in figure S13). When no equation of state is available (right column of figure S13) we kept the cell parameters at the highest pressure they have been retrieved. We note that the peak intensity is not expected to match data acquired on the powder-like sample as our sample is highly textured, also showing a columnar structure, and our azimuthal coverage is limited (see figure S1). We can see that none of the previously reported phases can explain the present observations and a α-Fe_2O_3 phase (named α'-Fe_2O_3) with adjusted cell parameter is best explaining the observed x-ray diffraction pattern.

K. Volume drop and Birch–Murnaghan low-pressure fit

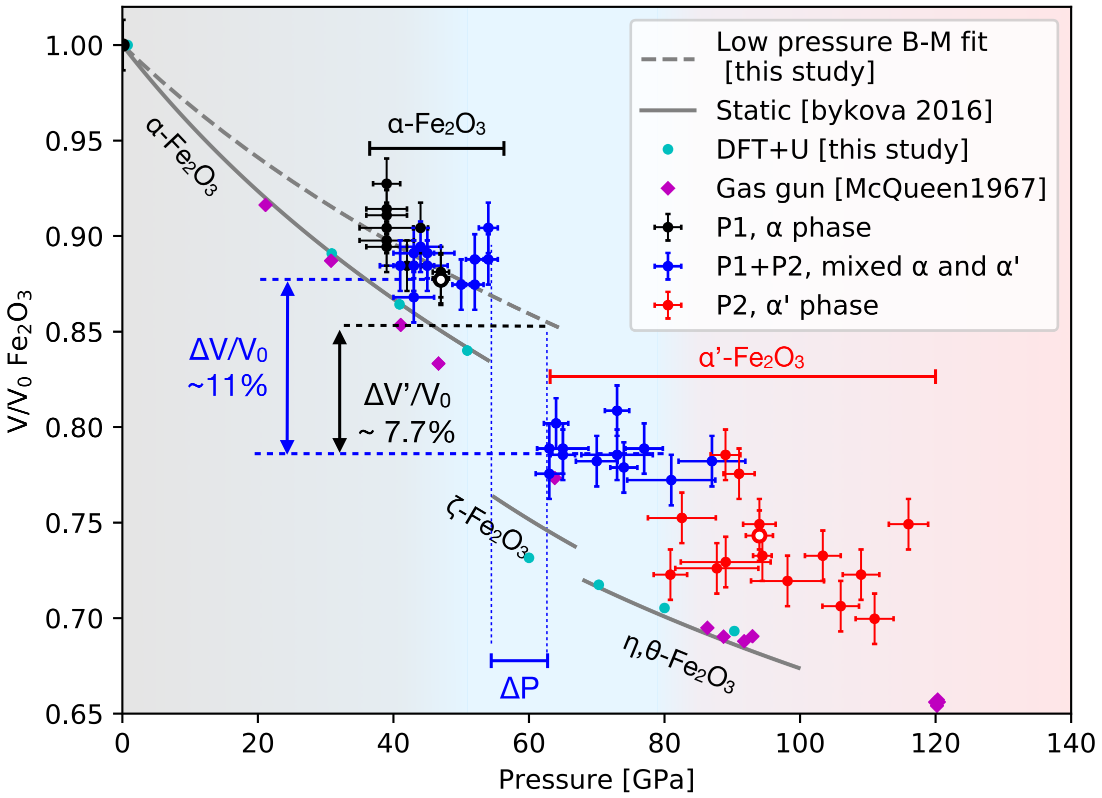

FIG. S14. V/V$_0$ for α-Fe$_2$O$_3$ and α'-Fe$_2$O$_3$ determined from x-ray diffraction as a function of pressure, compared with other published work. Points corresponding to the observation of only the α-Fe$_2$O$_3$ phase are plotted in black, of only the α'-Fe$_2$O$_3$ phase in red, and of the coexistence of both phases in blue. The two empty symbols correspond to data points determined from the Le Bail fits shown in Fig. 2 of main paper. A transition from α-Fe$_2$O$_3$ to α'-Fe$_2$O$_3$ phase is observed at 54-62 GPa. It is associated with a relative volume jump $\Delta V/V_0$ equal to 11.0 % and pressure jump of $\Delta P \sim 9$ GPa. A second-order Birch-Murnaghan fit (B-M fit represented with grey dashed line) has been performed for α phase. The relative volume jump between the extrapolated volume for α phase at 63-65 GPa and the measured volume for the α' phase at the same pressure is $\Delta V'/V$ =7.7%.

A 2nd Birch-Murnahan fit $P(V) = 3/2K_0[(V_0/V)^{2/3} - 1](V_0/V)^{5/3}$ (with V_0 constant equal to 303 Å^3) has been realized for the α phase (below 60 GPa). A K_0 of 292 GPa was determined which is higher than K_0 based on static compression experiments, e.g. 219 and 258 GPa in [14] and [19] respectively. This is due to the overall volume shift observed in the present dynamic compression data, whose origin is discussed in the main text. Moreover the data points are lying in a small pressure range (28-60 GPa) which makes the fitting arduous. Based on this fit the volume of the alpha phase at 63-65 GPa is found to be equal to (V/V_0=0.85). The volume jump between the extrapolated volume for alpha phase at 63-65 GPa and the measured volume for the α' phase at the same pressure ($\Delta V'/V_0$) is thus equal to 7% (against to 11% for the volume jump between the alpha phase and the α' phase reported here around the transition ($\Delta V/V_0$)). This volume jump remains significant and of the order of magnitude of typical spin transition volume jump.

L. DFT volume drop and spin transition; dependence on U

As our experimental data only show the α-Fe_2O_3 phase, the relaxation of cell parameters, atomic positions and magnetic state of iron was performed with $R\bar{3}c$ symmetry. Our simulations were performed using the v7.1 Quantum-Espresso suite [20, 21]. Scalar-Relativistic ultrasoft pseudopotential (PP) [22] were generated using the PBEsol exchange-correlation functionals [23] for Fe and O. The effective Hubbard U parameter was used for the Fe-3d orbitals, with the initial occupations given by the PP. We used a kinetic-energy cutoff of the plane-wave basis set of 100 Ry and an augmentation charge energy cutoff of 800 Ry. The calculations were carried out using a 12×12×12 $\boldsymbol{k}$-point grid. The DFT+U calculations were performed at ambient pressure using $U = 5$ eV, leading to an energy band gap of 2.075 eV and magnetic moment per Fe atom of 4.41 μ_B, in agreement with experimental values of 2.14 eV and 4.6 μ_b, respectively [24, 25].

The U parameter used in our calculations should a priori vary with pressure and temperature, although previous studies generally used a constant U [26, 27]. We therefore performed similar calculations for different values of U = 1, 3, 5, and 7 eV (see figure S15). Different values of U are changing the pressure of phase transition but it did not change the calculated volume drop of around 10% linked to the change from high to low spin.

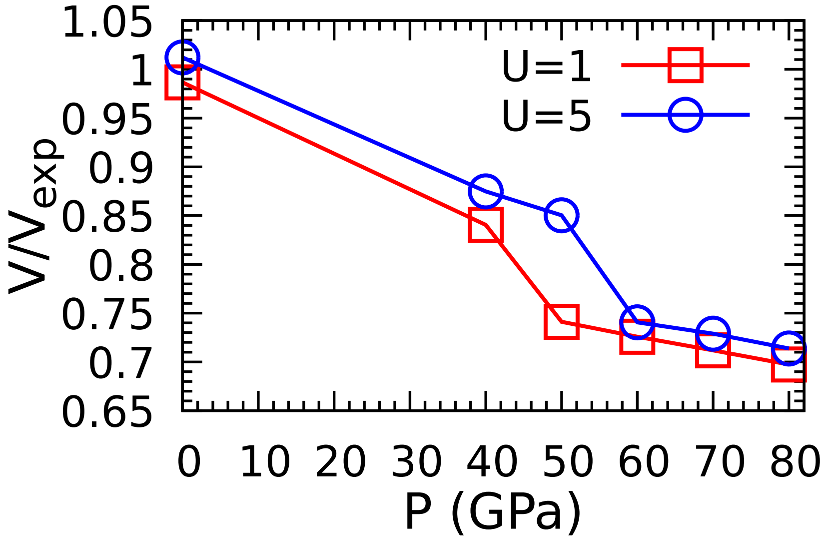

FIG. S15. Volume as a function of pressure obtained using DFT+U with two different values for U=1,5. $V_{\mathrm{exp}} = 100.58(3)\mathring{A}^3$ is the experimental volume at the ambient condition. DFT+U results with U=5 agree with the experiment.

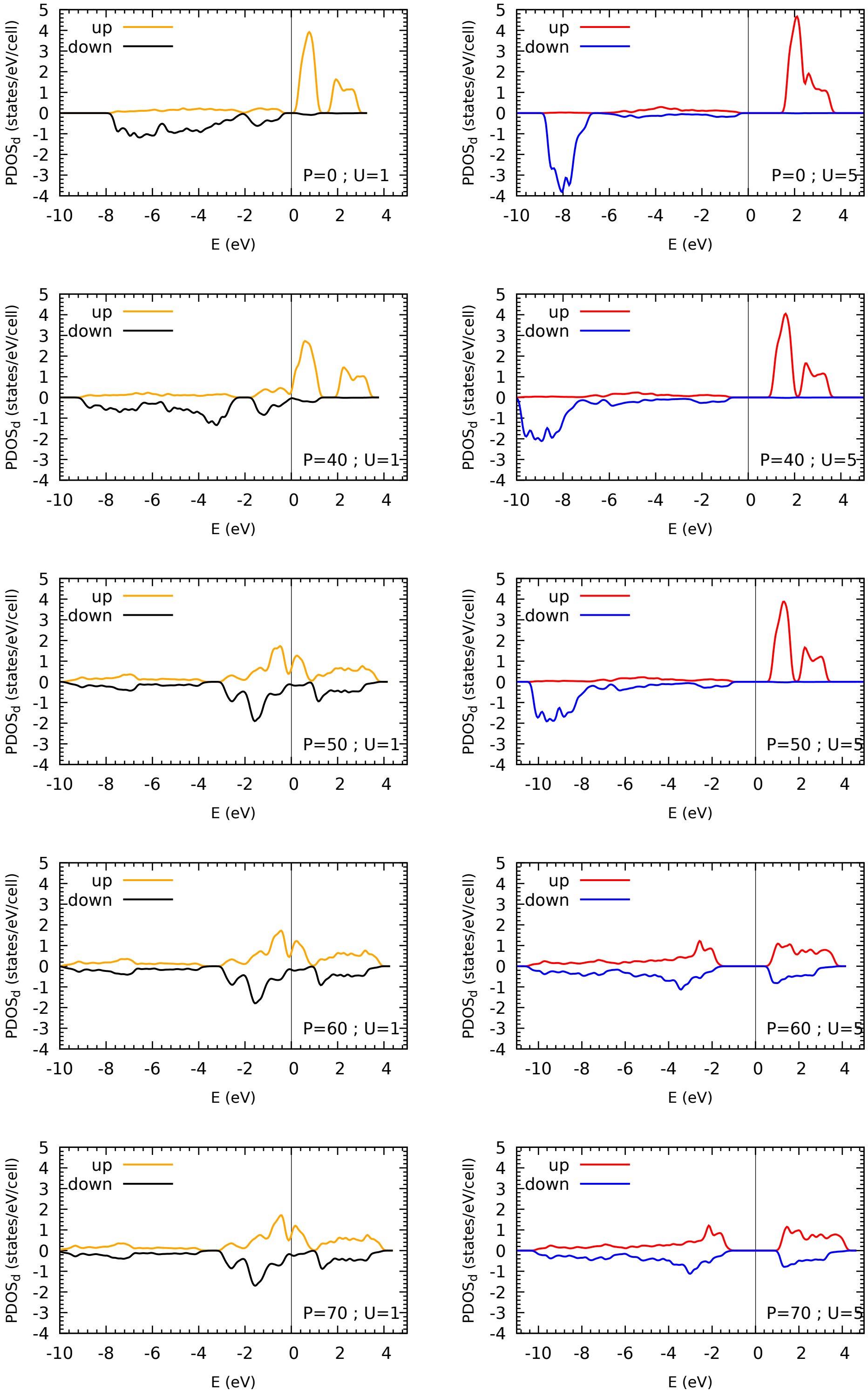

FIG. S16. Projected DOS of Fe-d orbital obtained using DFT+U with U=1,5 and at pressures P=0, 40, 50, 60, and 70 GPa. The vertical line presents the Fermi energy.

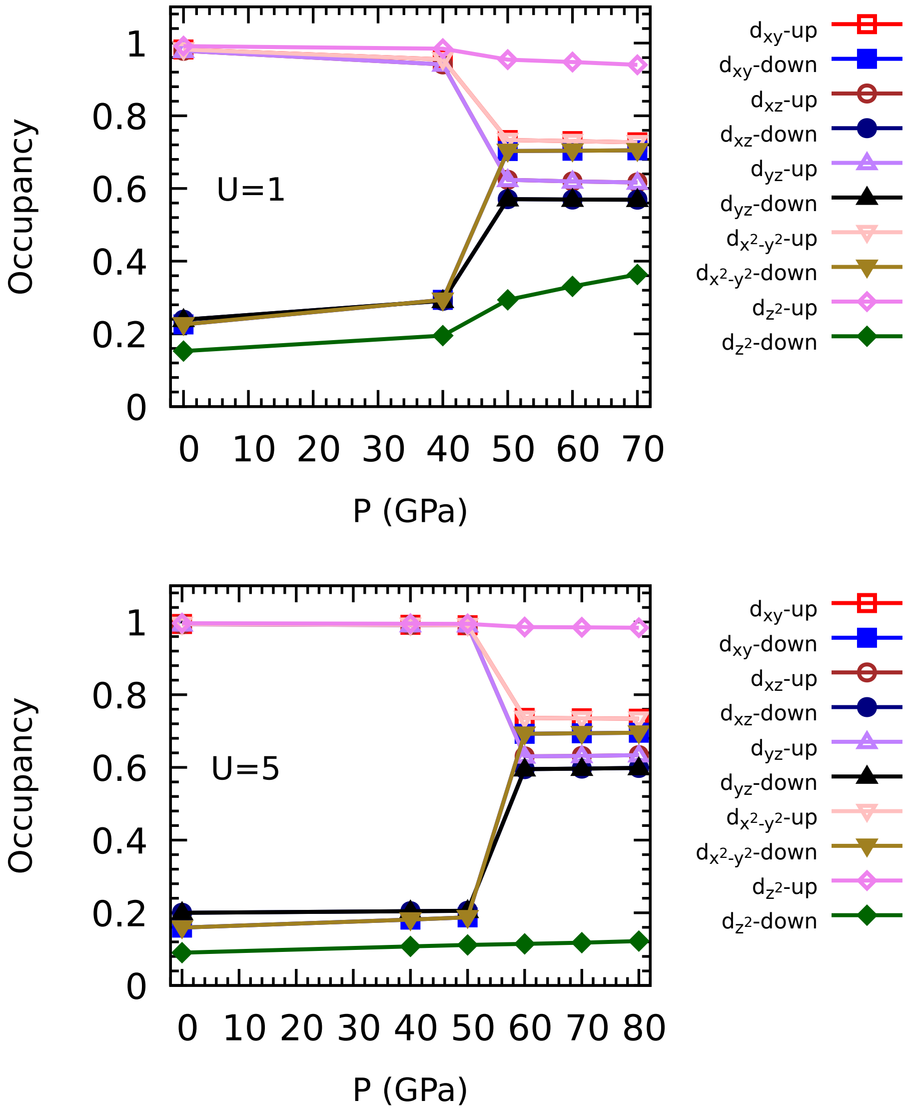

FIG. S17. Fe-d orbital occupancy as a function of pressure calculated with U=1, and 5 using Lowdin charge analysis.

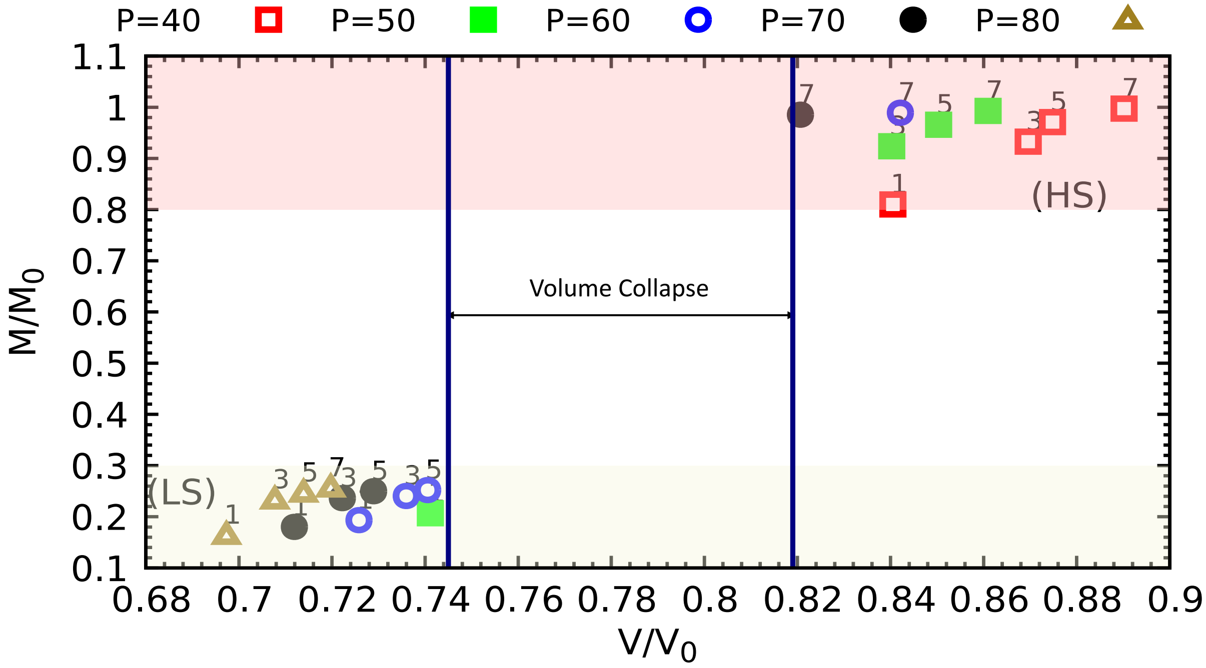

FIG. S18. Relative absolute magnetization M as a function of volume. M_0 and V_0 are magnetization and volume at the ambient conditions, respectively. The results are calculated at P=40, 50, 60, 70, and 80 GPa (data point above the plot) with U=1, 3, 5, and 7 (the values on top of the data point in the figure). The existence of high-spin (HS) to low-spin (LS) phase transition due to volume collapse is independent of the U parameter.

---

[1] A. Descamps, B. K. Ofori-Okai, O. Bistoni, Z. Chen, E. Cunningham, L. B. Fletcher, N. J. Hartley, J. B. Hastings, D. Khaghani, M. Mo, B. Nagler, V. Recoules, R. Redmer, M. Schörner, D. G. Senesky, P. Sun, H.-E. Tsai, T. G. White, S. H. Glenzer, and E. E. McBride, Evidence for phonon hardening in laser-excited gold using x-ray diffraction at a hard x-ray free electron laser, Science Advances **10**, eadh5272 (2024).

[2] L. Lutterotti, Maud (material analysis using diffraction) version 2.33, https://luttero.github.io/maud, (2010).

[3] R. Blake, R. Hessevick, T. Zoltai, and L. Finger, Refinement of the Hematite Structure, American Mineralogist **51**, 123 (1966).

[4] W. A. Dollase, Correction of intensities for preferred orientation in powder diffractometry: application of the March model, Journal of Applied Crystallography **19**, 267 (1986).

[5] R. Ramis, R. Schmalz, and J. Meyer-Ter-Vehn, Multi— a computer code for one-dimensional multigroup radiation hydrodynamics, Computer Physics Communications **49**, 475 (1988).

[6] X. Cao, Y. Wang, X. Li, L. Xu, L. Liu, Y. Yu, R. Qin, W. Zhu, S. Tang, L. He, C. Meng, B. Zhang, and X. Peng, Refractive index and phase transformation of sapphire under shock pressures up to 210 GPa, Journal of Applied Physics **121**, 115903 (2017).

[7] S. H. Glenzer, L. B. Fletcher, E. Galtier, B. Nagler, R. Alonso-Mori, B. Barbrel, S. B. Brown, D. A. Chapman, Z. Chen, C. B. Curry, F. Fiuza, E. Gamboa, M. Gauthier, D. O. Gericke, A. Gleason, S. Goede, E. Granados, P. Heimann, J. Kim, D. Kraus, M. J. MacDonald, A. J. Mackinnon, R. Mishra, A. Ravasio, C. Roedel, P. Sperling, W. Schumaker, Y. Y. Tsui, J. Vorberger, U. Zastrau, A. Fry, W. E. White, J. B. Hasting, and H. J. Lee, Matter under extreme conditions experiments at the Linac Coherent Light Source, Journal of Physics B: Atomic, Molecular and Optical Physics **49**, 092001 (2016).

[8] Y. B. Zel'dovich and Y. P. Raizer, Shock waves in solids, in *Physics of Shock Waves and High-Temperature Hydrodynamic Phenomena* (Elsevier, 1967) pp. 685–784.

[9] R. McQueen and S. Marsh, Handbook of Physical Constants (unpublished data), Geological Society of America Memoir **97**, 153 (1966).

[10] A. Flacco and T. Vinci, https://github.com/neutrinotoolkit/neutrino, (2013).

[11] T. De Rességuier, P. Berterretche, and M. Hallouin, Influence of quartz anisotropy on shock

propagation and spall damage, International Journal of Impact Engineering **31**, 545 (2005).

[12] M. G. Gorman, A. L. Coleman, R. Briggs, R. S. McWilliams, D. McGonegle, C. A. Bolme, A. E. Gleason, E. Galtier, H. J. Lee, E. Granados, M. Śliwa, C. Sanloup, S. Rothman, D. E. Fratanduono, R. F. Smith, G. W. Collins, J. H. Eggert, J. S. Wark, and M. I. McMahon, Femtosecond diffraction studies of solid and liquid phase changes in shock-compressed bismuth, Scientific Reports **8**, 16927 (2018).

[13] C. Crépisson, A. Amouretti, M. Harmand, C. Sanloup, P. Heighway, S. Azadi, D. McGonegle, T. Campbell, J. Pintor, D. A. Chin, E. Smith, L. Hansen, A. Forte, T. Gawne, H. J. Lee, B. Nagler, Y. Shi, G. Fiquet, F. Guyot, M. Makita, A. Benuzzi-Mounaix, T. Vinci, K. Miyanishi, N. Ozaki, T. Pikuz, H. Nakamura, K. Sueda, T. Yabuuchi, M. Yabashi, J. S. Wark, D. N. Polsin, and S. M. Vinko, Shock-driven amorphization and melting in Fe2O3, Physical Review B **111**, 024209 (2025).

[14] E. Bykova, L. Dubrovinsky, N. Dubrovinskaia, M. Bykov, C. McCammon, S. V. Ovsyannikov, H. P. Liermann, I. Kupenko, A. I. Chumakov, R. Rüffer, M. Hanfland, and V. Prakapenka, Structural complexity of simple Fe_2O_3 at high pressures and temperatures, Nature Communications **7**, 10661 (2016).

[15] L. S. Dubrovinsky, N. A. Dubrovinskaia, C. McCammon, G. K. Rozenberg, R. Ahuja, J. M. Osorio-Guillen, V. Dmitriev, H.-P. Weber, T. L. Bihan, and B. Johansson, The structure of the metallic high-pressure Fe_3O_4 polymorph: experimental and theoretical study, Journal of Physics: Condensed Matter **15**, 7697 (2003).

[16] Q. Hu, D. Y. Kim, W. Yang, L. Yang, Y. Meng, L. Zhang, and H.-K. Mao, FeO_2 and FeOOH under deep lower-mantle conditions and Earth's oxygen–hydrogen cycles, Nature **534**, 241 (2016).

[17] B. Lavina and Y. Meng, Unraveling the complexity of iron oxides at high pressure and temperature: Synthesis of Fe_5O_6, Science Advances **1**, e1400260 (2015).

[18] B. Lavina, P. Dera, E. Kim, Y. Meng, R. T. Downs, P. F. Weck, S. R. Sutton, and Y. Zhao, Discovery of the recoverable high-pressure iron oxide Fe_4O_5, Proceedings of the National Academy of Sciences **108**, 17281 (2011).

[19] G. K. Rozenberg, L. S. Dubrovinsky, M. P. Pasternak, O. Naaman, T. Le Bihan, and R. Ahuja, High-pressure structural studies of hematite Fe_2O_3, Physical Review B **65**, 064112 (2002).

[20] P. Giannozzi and et al., Quantum espresso: a modular and open-source software project for

quantum simulations of materials, Journal of physics: Condensed matter **39**, 395502 (2009).

[21] P. G. et al., Advanced capabilities for materials modelling with quantum espresso, J. Phys.: Condens. Matter **29**, 465901 (2017).

[22] A. D. Corso, Pseudopotentials periodic table: From h to pu, Computational Materials Science **95**, 337 (2014).

[23] J. P. Perdew, A. Ruzsinszky, G. I. Csonka, O. A. Vydrov, G. E. Scuseria, L. A. Constantin, X. Zhou, and K. Burke, Restoring the density-gradient expansion for exchange in solids and surfaces, Phys. Rev. Lett. **100**, 136406 (2008).

[24] D. Benjelloun, J.-P. Bonnet, J.-P. Doumerc, J.-C. Launay, M. Onillon, and P. Hagenmuller, Mater. Chem. Phys. **10**, 503 (1984).

[25] J. M. D. Coey and G. A. Sawatzky, J. Phys. C **4**, 2386 (1971).

[26] E. Greenberg, I. Leonov, S. Layek, Z. Konopkova, M. P. Pasternak, L. Dubrovinsky, R. Jeanloz, I. A. Abrikosov, and G. K. Rozenberg, Pressure-Induced Site-Selective Mott Insulator-Metal Transition in Fe_2O_3, Physical Review X **8**, 031059 (2018).

[27] D. B. Ghosh and S. de Gironcoli, Structural and spin transitions in Fe_2O_3, arXiv:0903.2104 [cond-mat] (2009), arXiv: 0903.2104.